

# Physical-mechanical characterization of biodegradable Mg-3Si-HA composites

Chander Prakash and Sunpreet Singh

*School of Mechanical Engineering, Lovely Professional University, Punjab, India*

Ilenia Farina

*Department of Engineering, University of Naples, Naples, India, and*

Fernando Fraternali and Luciano Feo

*Department of Civil Engineering, University of Salerno, Italy*

152

Received 28 April 2018  
Accepted 13 July 2018

## Abstract

**Purpose** – Porous implant surface is shown to facilitate bone in-growth and cell attachment, improving overall osteointegration, while providing adequate mechanical integrity. Recently, biodegradable material possessing such superior properties has been the focus with an aim of revolutionizing implant's design, material and performance. This paper aims to present a comprehensive investigation into the design and development of low elastic modulus porous biodegradable Mg-3Si-5HA composite by mechanical alloying and spark plasma sintering (MA-SPS) technique.

**Design/methodology/approach** – This paper presents a comprehensive investigation into the design and development of low elastic modulus porous biodegradable Mg-3Si-5HA composite by MA-SPS technique. As the key alloying elements, HA powders with an appropriate proportion weight 5 and 10 are mixed with the base elemental magnesium (Mg) particles to form the composites of potentially variable porosity and mechanical property. The aim is to investigate the performance of the synthesized composites of Mg-3Si together with HA in terms of mechanical integrity hardness and Young's moduli corrosion resistance and *in-vitro* bioactivity.

**Findings** – Mechanical and surface characterization results indicate that alloying of Si leads to the formation of fine Mg<sub>2</sub>Si eutectic dense structure, hence increasing hardness while reducing the ductility of the composite. On the other hand, the alloying of HA in Mg-3Si matrix leads to the formation of structural porosity (5-13 per cent), thus resulting in low Young's moduli. It is hypothesized that biocompatible phases formed within the composite enhanced the corrosion performance and bio-mechanical integrity of the composite. The degradation rate of Mg-3Si composite was reduced from 2.05 mm/year to 1.19 mm/year by the alloying of HA elements. Moreover, the fabricated composites showed an excellent bioactivity and offered a channel/interface to MG-63 cells for attachment, proliferation and differentiation.

**Originality/value** – Overall, the findings suggest that the Mg-3Si-HA composite fabricated by MA and plasma sintering may be considered as a potential biodegradable material for orthopedic application.

**Keywords** Silicon, Hydroxyapatite, Elastic modulus, Magnesium composite, Mechanical alloying, Spark plasma sintering

**Paper type** Research paper



© Chander Prakash, Sunpreet Singh, Ilenia Farina, Fernando Fraternali and Luciano Feo. Published in *PSU Research Review*. Published by Emerald Publishing Limited. This article is published under the Creative Commons Attribution (CC BY 4.0) licence. Anyone may reproduce, distribute, translate and create derivative works of this article (for both commercial and non-commercial purposes), subject to full attribution to the original publication and authors. The full terms of this licence may be seen at <http://creativecommons.org/licenses/by/4.0/legalcode>

## 1. Introduction

The increased demand of an artificial organ, hard tissue replacements and bone fixation devices led to the design and development of a wide range of new biomaterials. Commonly used yet successful are stainless steel, cobalt-chromium, titanium and its composites, which possess superior bio-mechanical properties and integrity (Geetha *et al.*, 2009). However, it has been witnessed that their full potential use is not escalating and, often hindered because of the consequential drawbacks. For instance, first, the elastic modulus of these materials is much higher (110-200 GPa) than that of the bone (10-45 GPa), which causes stress shielding (Prakash *et al.*, 2016). As a result, the bone resorption occurs, leading to implant loosening and failure. Second, biomaterials are used as long-lasting bone fixation devices or implants. Spoerke *et al.* (2005) reported that after the bone healing, the implants must be removed from the body by a secondary surgical procedure, causing an increased healthcare cost, and mental stress toward the patients. In light of the issues around the existing hard metal implants, magnesium (Mg)-based composites are gaining a growing attention as a promising alternative for bio-inserts and bone fixation devices, because of their high biodegradability, superior biocompatibility and low elastic modulus nearing to that of the bone (Staiger *et al.*, 2006). Uddin *et al.* (2015) reported that Mg was degraded very rapidly after implantation in the human body. Over the decades, numerous methodology and progressive techniques have been employed to regulate the deterioration rate in a way such that the implant provides adequate mechanical integrity until the complete bone healing (Uddin *et al.*, 2015 and Uddin *et al.*, 2017). This has been a pressing challenge for biomedical engineers and material scientists, aiming to explore the potential solutions to produce implants with the controlled degradation ability. Zhang *et al.* (2009) reported that the element alloying was found the most successful and potential method to control the degradation rate of Mg composites. Radha and Sreekanth (2017) critically conducted the review on the development of magnesium alloys, in which, elements, for example, Zn, Al, Ag, Y, Zr, Nd, Si, Mn, TiO<sub>2</sub> and Ca, were selected in the response of their biological function in the human body. While the element Al in Mg-composites improves mechanical properties, but Al<sup>+</sup> ions released cause Alzheimer's disease and muscle fiber damage (Zhang *et al.*, 2012; Gu *et al.*, 2011; Zhang *et al.*, 2012). Song (2007) reported that Zr causes very serious diseases such as lung cancer, liver cancer, and breast cancer. Zhang *et al.* (2012) reported that the alloying of Nd and Y in Mg-alloy disrupt the growth of tissues around the implant. Li *et al.* (2008) observed that the alloying of Ca reduced the degradation rate and improved bio-mechanical integrity in a corrosive media. Moreover, Ca is a main and prime element of human bone, which stimulates the bone ingrowth process, thus accelerating the bone healing (Khanra *et al.*, 2010). The alloying of Zn and Mn in the Mg matrix enhanced both elasticity and corrosion resistance (Gu *et al.*, 2010). Recently, Ben-Hamu *et al.* (2007) reported that Si has proved to be an imperative element being alloyed to develop tissues. The developed Mg-Si composites showed low ductility, high strength and high corrosion resistance because of the presence of bigger Mg<sub>2</sub>Si particle and eutectic phases. In this regard, various manufacturing techniques, such as conventional sintering, have been used to fabricate Mg and its composites (Vahidgolpayegani *et al.*, 2017). However, the shortcomings of the techniques are, for example, long sintering time and high temperature, which degrades mechanical and electrochemical properties, and thus, the fabricated devices have failed in long-term under cyclic loading. Spark plasma sintering (SPS) technique has been accounted for a novel and intense approach to fabricate porous compact with improved mechano-biological, antibacterial and corrosion performance. The SPS is a powder metallurgy, and the consolidation of powders by sintering uses a shorter holding time, a relatively lower sintering temperature and a high pressure at the rapid heating and cooling

rates ( $>100^{\circ}\text{C}/\text{min}$ ). [Table I](#) presents a summary of the current literature on the fabrication of Mg-alloy using SPS.

It is clear that many studies, in the past, reported on design, development and synthesis of Mg-alloy alloyed with Mn, and Zn using various fabrication techniques, with the aim of controlling the degradation rate. However, to the best knowledge of the authors, no research study is available, reporting on the combined effect of Si and HA addition in Mg-alloy on elastic modulus, corrosion resistance and bioactivity, as can be seen in [Table I](#). To this end, the current paper aims to study the synthesis, characterization, corrosion and cell response of Mg-3Si-HA composite fabricated via MA-SPS technique. The key expectation is that the fabricated porous bio-alloy will exhibit improved bio-mechanical integrity while offering increased corrosion resistance to delay the degradation and bioactivity for bone fixation and orthopedic applications.

## 2. Material and method

### 2.1 Mechanical alloying and consolidation of spark plasma sintering

High purity ( $\sim 99.9$  per cent) elements Mg, Si and HA were used to prepare Mg-3Si-HA composites. The chemical composition of the proposed composites in weight per cent is listed in [Table II](#). [Figure 1](#) shows the shape and size of powder particles before mechanical alloying (MA). The HA powder particles have an average particle size of  $0.5\ \mu\text{m}$  with irregular shape, whereas the other powder particles exhibited an average size of  $25\ \mu\text{m}$  with spherical morphology. The required powders were weighed and MA was carried out by using high-energy planetary ball mill (Make: Fritsch, Pulverisette 7). The stainless steel vial with stainless steel balls (of diameter of 5 mm) was used. The powder mixture was alloyed for 12 h with a ball-to-powder ratio of 10:1 at a rotational speed of 300 rpm. The blended powders are first pre-heated at  $200^{\circ}\text{C}$  for 2 h in an argon gas atmosphere to dissipate the dampness and then solidified via SPS technique using a SPS-5000 machine (Model: Dr Sinter SPS-625, Fuji Electronic Industrial Co. Ltd., Japan). The SPS was carried out with a heating rate of 50 K/min (holding time 5 min) under vacuum conditions at sintering temperatures of  $400^{\circ}\text{C}$  and applied pressure of 40 MPa, as per the procedure followed by [Singh et al. \(2017\)](#).

A graphite die was used for the sintering of powder's mixture and solid compacts of the diameter of 20 mm and thickness of 4 mm were synthesized. The objective of changing temperature and pressure was to investigate its effect on structural porosity and density. [Figure 2\(a\)](#) shows the schematic representation of SPS technique. During SPS process, thermal energy generated due to electrical sparks between the powder particles and the contact area causes partial melting of the grain boundary of powder while uniaxial applied pressure densifies the powder mixture [[Figure. 2\(b\)](#)]. The process of densification and solidification forms the final sintered compact. [Figure 2\(c\)](#) shows the mass transformation during the SPS and the phenomena of partial diffusion and welding of powder particles ([Zheng et al., 2011](#)). Sintering pressure enables to get rid of pores and induces an additional driving force for the compaction. On the other hand, high sintering temperature assists the powder particles to coalesce, which subsequently reduces the porosity and densifies the compact ([Talò et al., 2017](#); [Carni et al., 2017](#); [Ermakova and Dayyani, 2017](#); [Fraddosio et al., 2017](#)).

### 2.2 Microstructure and mechanical properties

The percentage of structural porosity was calculated by Archimedes method using water. First samples' mass was weighed and then immersed in the small beaker. The weight of the sample in water was measured, whereby the loss of weight of the sample when suspended in water was equal to the mass of fluid displaced, from which its volume and hence open porosity could be calculated using formula:

| Author and year             | Alloy/composite composition            | Observations  | <i>In-vitro/ in-vivo</i> analysis   |
|-----------------------------|--|---|---|
| Sunil <i>et al.</i> 2014    | Biodegradable Mg- $\times$ HA implants | Mg-10% HA composite exhibit best corrosion resistance and high hardness   | Not studied   |
| Zheng <i>et al.</i> 2011    | Mg-Al-Zn alloy                         | As sintered Mg-Al-Zn alloy possessed maximum microhardness of 140 HV, compressive yield strength of 442.3 MPa, and ultimate strength of 546MPa, which comparatively higher than that of values of conventional Mg alloys  | Not studied   |
| Lala <i>et al.</i> 2017     | Mg-Mn-Zn doped HAP alloy               | The as sintered alloy exhibit high hardness of 13 GPa and brittle index   | Not studied   |
| Zhang <i>et al.</i> 2010    | Mg-Si(-Ca, Zn) alloy                   | The addition of Ca and Zn to Mg-Si alloy improved the bio-corrosion resistance and showed very good biocompatibility.   | <i>In-vitro</i> analysis revealed that excellent adhesion and growth of osteoblastic cell have been observed and <i>in-vivo</i> results suggested the alloy had good biocompatibility |
| Liu <i>et al.</i> 2016      | Zn-Mg-Mn alloy                         | The as fabricated alloy after rolling significantly improved its mechanical properties, corrosion resistance and bioactivity  | Adhesion and growth of osteoblastic cell have been observed   |
| Fu <i>et al.</i> 2017       | Mg-Zn-Mn-Ca alloys                     | The as sintered alloy exhibits 58-69 MPa yield strength, 177-205 MPa Tensile strength and 49-53 Hv hardness   | Not studied   |
| Rudinsky <i>et al.</i> 2016 | Al-Zn-Mg alloy                         | The as sintered alloy exhibits 91 HV microhardness and 659 MPa flexural strength  | Not studied   |
| Tünçay <i>et al.</i> 2017   | Al-Zn-Mg-Cu                            | Al-Zn-Mg-Cu alloy was fabricated with relative density of 99.1-99.8% and microhardness of $173 \pm 3$ and $172 \pm 3$ HV, respectively  | Not studied   |
| Chen <i>et al.</i> 2009     | Al-Zn-Mg-Cu                            | Nano grained Al-Zn-Mg-Cu alloy was fabricated   | Not studied   |
| Cao <i>et al.</i> 2017      | Mg- $\times$ ZnO                       | The findings suggested that as fabricated Mg-10 Wt. % ZnO composite has excellent biocorrosion resistance properties and potential candidate for temporary implant application. Moreover, the ZnO powder enhanced the strength and the ductility of the fabricated composites   | Not studied   |
| Narita <i>et al.</i> 2016   | Mg/ $\beta$ - TCP composites           | The densification of Mg/ $\beta$ - TCP composites possessed excellent mechanical properties and high hardness   | Not studied   |
| Cheng <i>et al.</i> 2017    | Pure-Mg                                | The results indicated that the densification of pure Mg can be improved by the reduction of particle size, suggesting the intrinsic driving force, local pressure and current intensity were enhanced significantly by a decrease in the particle size at the same sintering conditions, which can promote shrinkage of pores, formation of the sintering neck and mass transportation in the SPS process | Not studied   |

(continued)

**Table I.**  
Brief summary of the research work done in fabrication of magnesium-based alloys and composite using spark plasma sintering process

| Author and year            | Alloy/composite composition     | Observations   | <i>In-vitro/ in-vivo</i> analysis |
|----------------------------|---------------------------------|--|-----------------------------------|
| Queudet <i>et al.</i> 2017 | Al-Zn-Mg Alloy                  | The nano-grained Al-Zn-Mg Alloy Was fabricated, which has high compressive strength and hardness 830 MPa and 196 HV, respectively  | Not studied                       |
| Ghasali <i>et al.</i> 2017 | Mg-5%B <sub>4</sub> C           | Mg-5%B <sub>4</sub> C was fabricated by microwave sintering and SPS technique. The SPS samples possessed higher bending strength (191 ± 15 MPa) and microhardness (92 ± 7 Vickers) than microwave samples  | Not studied                       |
| Knotek <i>et al.</i> 2017  | Mg-Ni alloys                    | The Mg-25% Ni alloys were fabricated, which ensures best hydriding performance and dehydriding temperature is decreased with increasing Ni content   | Not studied                       |
| Zhang <i>et al.</i> 2017   | Mg-Al-nanoSiC                   | Then reinforced Mg-1Al-xSiC (x = 0.3, 0.6, 1.2, 2.4 Wt.%) composites were successfully fabricated by spark plasma sintering (SPS) followed by hot extrusion. The Mg-1Al-1.2SiC composite exhibited higher 0.2% tensile yield strength (176 MPa vs 98 MPa, increased by ~80%), ultimate tensile strength (246 MPa vs 188 MPa, increased by ~31%), 0.2% compressive yield strength (140 MPa vs 81 MPa, increased by ~73%) and ultimate compressive strength (338 MPa vs 255 MPa, increased by ~33%) without much reduction on failure strain | Not studied                       |
| Knotek <i>et al.</i> 2017  | Mg-Ni-X (X = Co, Mn, Nd) alloys | Highly porous Mg-Ni-X (X = Co, Mn, Nd) alloys were fabricated by SPS technique. The highest total amount of hydrogen was absorbed by the MgNi <sub>26</sub> Nd <sub>10</sub> alloy, nearly 1.8 Wt.%. The main hydriding product was the binary hydride MgH <sub>2</sub>  | Not studied                       |

**Table I.**

To investigate the morphology and elemental composition, the samples were cut from the as-sintered compacts. The samples were finished with silicon carbide emery papers and well-polished up to surface roughness  $R_a$  of 0.5  $\mu\text{m}$ . Micro-structure, morphology, elemental and phase composition of the samples were investigated by field emission scanning electron microscopy (FE-SEM; JEOL 7600F), energy dispersive spectroscopy (EDS) and XRD technique, respectively. The Young's modulus is the basic characteristics of the biomaterial and is of the interest to determine mechano-biological stability. Thus, elastic modulus and hardness were determined via nanoindentation tests (Hyistron TI-950 indentation system) using the Oliver-Pharr method, as reported by [Oliver and Pharr \(1992\)](#). The Berkovich tip was used for the indentation with a maximum applied load of 1,000  $\mu\text{N}$  intensity.

### 2.3 Corrosion resistance

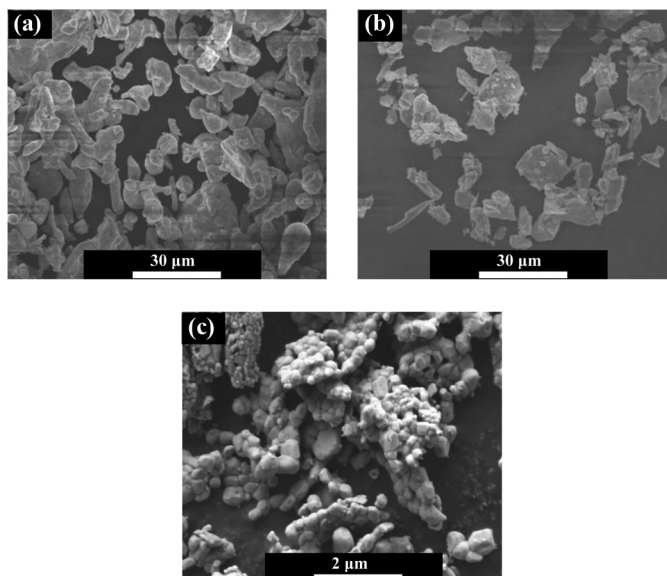
The corrosion behavior and degradation rate were assessed via electrochemical potentiodynamic workstation (DC potentiostat/galvanostat model, Auto Lab PGSTAT30, Netherlands). To mimic the human body fluid condition, Ringer's solution as a simulated body fluid (SBF) was used as an electrolyte. The polarization behavior

was monitored after 24-h immersion of the specimens in SBF with the scan rate of  $0.001 \text{ Vs}^{-1}$ . Three-electrode cell was used equipped with the specimen as a working electrode, the graphite rod as a counter electrode and Ag/AgCl saturated calomel as a reference electrode. The corrosion parameters were determined from the Tafel plot using Stern-Geary, as per ASTM standard G102-89, as per the procedure adopted by Prakash and Uddin (2017).

#### 2.4 Degradation analysis in simulated body fluid immersion

The degradation rate of as-fabricated Mg-composites was assessed by immersion test in SBF solution for 3, 7 and 14 days. The samples were well polished and dipped into SBF solution in sterilized vials as per the ASTM-G31-72 standard. After predetermined time period of immersion, the samples were retrieved from glass vial, washed with distilled water and dried into desiccators for 24 h. The degradation rate of samples was evaluated by the mass loss in SBF solution due to  $\text{Mg}^{2+}$  ion release. The degraded surface morphology of samples was analyzed using FE-SEM and EDS technique.

| Group | Composite  | Alloying element composition, Wt. % |    |      | Mg | <b>Table II.</b><br>Composition of<br>alloying elements in<br>weight per cent as<br>proposed for<br>composites |
|-------|------------|-------------------------------------|----|------|----|--|
|       |            | Si                                  | HA |      |    |  |
| I     | Mg-3Si     | 3                                   | –  | Bal. |    |  |
| II    | Mg-3Si-5HA | 3                                   | 5  | Bal. |    |  |
| III   | Mg-3Si-5HA | 3                                   | 10 | Bal. |    |  |



**Notes:** (a) Magnesium; (b) silicon; (c) hydroxyapatite

**Figure 1.**  
SEM micrograph and  
EDS spectrum  
showing the  
morphology and  
element composition  
of raw powders

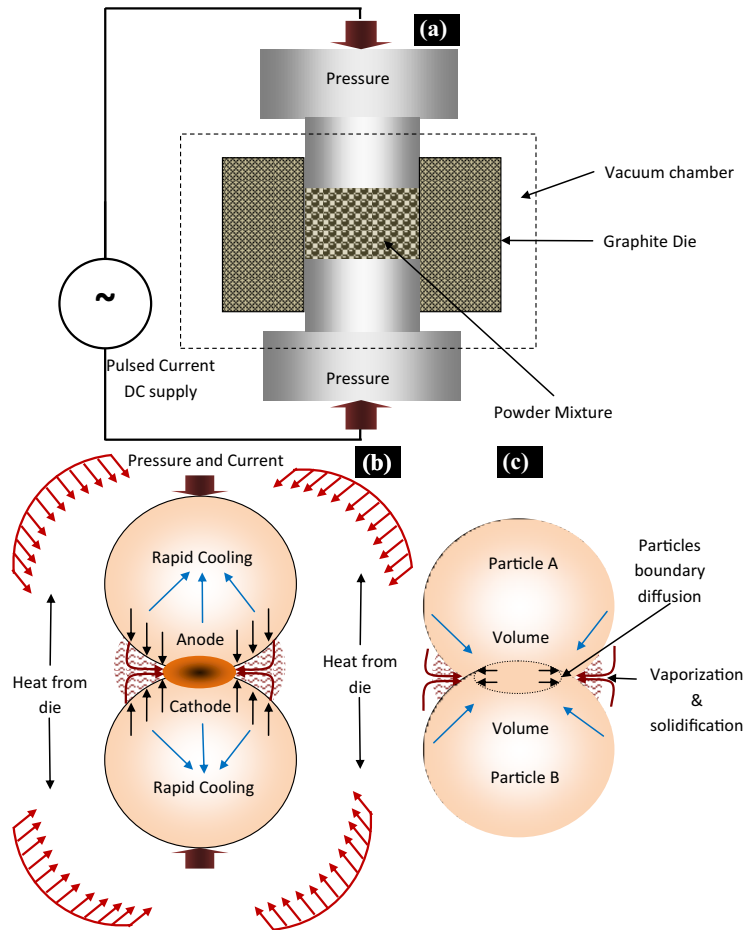


**Figure 2.**  
Mechanism of  
sintering of powder  
particles during SPS

### 2.5 *In-vitro* bioactivity analysis

The bioactivity of the fabricated composites was assessed by *in-vitro* cell culture tests. The disc type test specimens of size  $\phi 5 \times 3$  mm were cut from the as-sintered composites and placed in a 96-well plate. The MG-63 human osteoblast-like cells were seeded at an initial density of  $1 \times 10^5$  cells/cm<sup>2</sup> on to the samples and incubated at 37°C in a 5 Vol.% CO<sub>2</sub> atmosphere. After a predetermined time period of one, three and seven days, the cells were disengaged by trypsinization and the density was determined by hemocytometer under an optical microscope. Live and dead assays were performed to determine the cell viability on test specimens using an Olympus  $\times 51$  fluorescence microscopy. The cell adhesion onto the surface was observed under FE-SEM after the fixation, following a protocol adopted by Prakash and Uddin (2017). The cell proliferation was evaluated by MTT assay for cell culture period of one, three and seven days. Cell differentiation was evaluated by performing an alkaline phosphatase (ALP) activity. Three samples were used in each group by reporting the results as

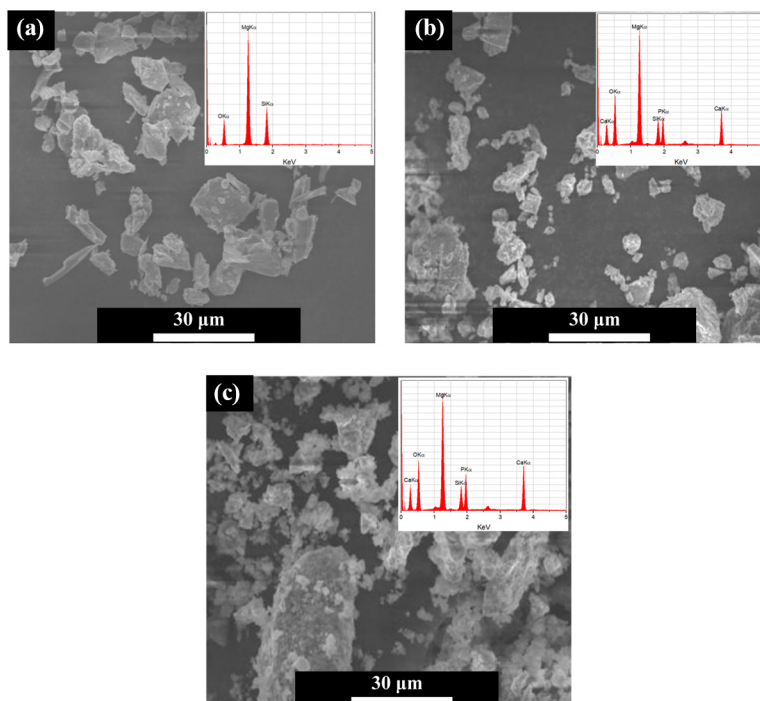
means  $\pm$  standard deviations. One-way analysis of variance (ANOVA) was performed considering  $p < 0.05$  statistically significant.

### 3. Results and discussion

#### 3.1 Microstructure characterization

The net weight of powder mixture before and after MA was approximately 10 gm, clearly indicating that there is no loss of powder. The change in particle size and morphology is a function of milling time. After milling for 8 h, the powder is reduced in size notably, and becomes irregular in shape. The reduction in grain size was because of plastic deformation and fragmentation in milling. After milling, the powder particles were completely homogenized, as can be seen in [Figure 3](#). Furthermore, it is observed that the powder particles were not defused with each other because of the localized temperature raised for a long time. [Zheng et al. \(2011\)](#) reported similar finding when Mg particles were milled with Al and Cu for more than 10 h. [Figure 3](#) shows the SEM morphology and associated EDS spectrum of mechanically alloyed powder after 8 h. It can be clearly seen that the HA powder is adhered on the Mg powder surface and powder sample is completely homogenized. The EDS spectrum presents the all-alloying elements only; no contamination takes place.

[Figure 4](#) presents the EDS spectrum and digital image of the as-sintered composites. The macro-scale image of composites revealed that the samples were fully consolidated without



**Notes:** (a) Mg-3Si; (b) Mg-3Si-5HA; (c) Mg-3Si-10HA

**Figure 3.**  
Powder morphology  
and size after ball  
milling for 8 h

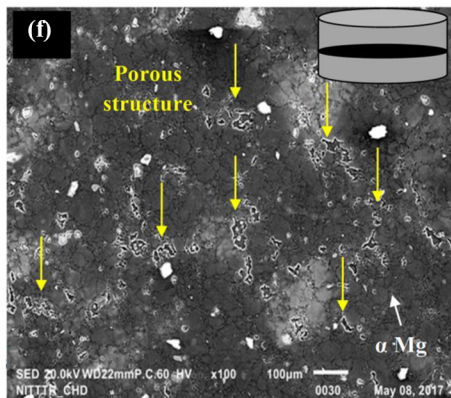
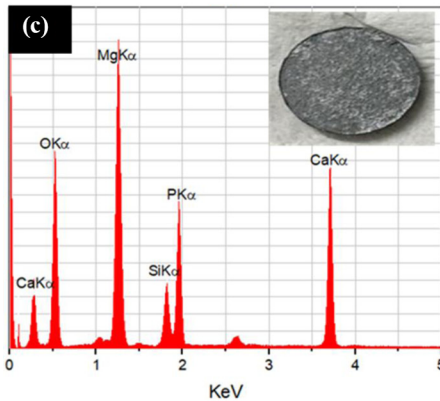
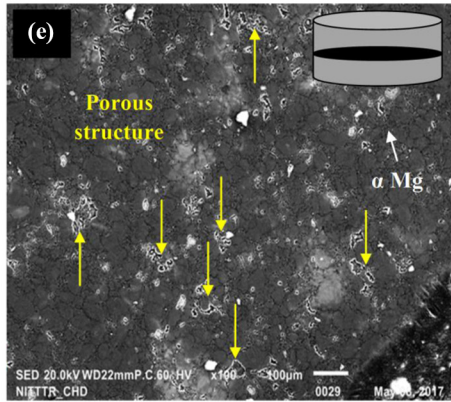
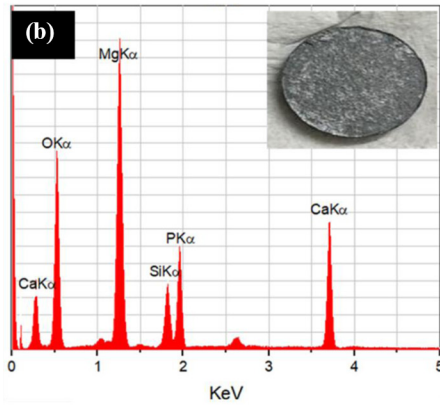
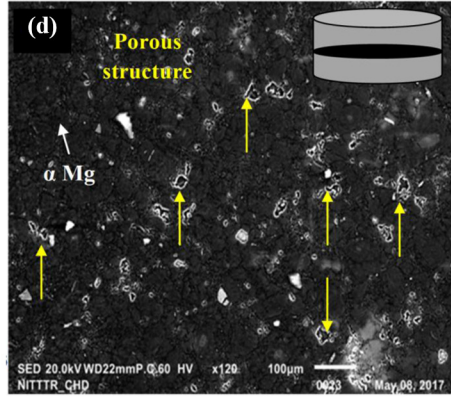
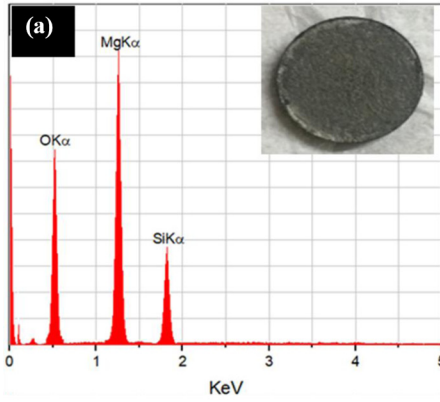


**Figure 4.** Photograph and associated EDS spectrum of composites pallets sintered at 40 MPa applied pressure and 400°C sintering temperature

**Notes:** (a) Mg-3Si; (b) Mg-3Si-5HA; (c) Mg-3Si-10HA temperature

any surface cracks or fracture. The high melting temperature of HA ( $\sim 1,100^\circ\text{C}$ ) does not allow its particle to react/interact with the other alloying elements at lower sintering temperature of  $400^\circ\text{C}$ . The EDS spectrum of Mg-3Si composite revealed the presence of Mg, Si and O elements in structure, as can be seen in Figure 4(a). The EDS spectrum of Mg-3Si-5HA composite revealed the presence of Ca and P along with Mg, Si and O elements in structure, as can be seen in Figure 4(b). The peaks intensity ration of Ca and P is 1.69, which is desirable in the composition. Similarly, Figure 4(c) presents the EDS spectrum of Mg-3Si-10HA composite. The peaks intensity of Ca and P is high as compared to Mg-3Si-5HA composite and their ration is still 1.69. Figure 4(d-f) shows the SEM micrograph of the transverse cross-section of all sintered composite compacts. Open pore structure can be clearly seen from the micrographs. During SPS processing, a large amount of gases was discharged because of heat generation, which results in the formation of porosity. Moreover, SEM micrographs indicate the formation of a distinct structure within the composites – dark, grey and bright phases in Mg matrix. The dark phase is  $\alpha$ -Mg primary grain boundary, grey represents the Si element and bright phase represents the HA elements. The Mg-3Si composite compact has less structural porosity (3-5 per cent). The Mg-3Si-5HA composite has higher degree of structural porosity (8-10 per cent) than Mg-3Si composite has, whereas, Mg-3Si-10HA composite has highest degree of structural porosity than Mg-3Si-5HA and Mg-3Si composites have. As a consequence, the porosity generation results into the reduction of density of the compact. Correspondingly, the theoretical density of all sintered composites was calculated by the rule of mixture. Table III shows the theoretical and measured density of the composites. It can be clearly seen that Mg-3Si composite sample has porosity 3.5 per cent only, which reveals that sample is fully sintered and densified, whereas, Mg-3Si-5HA composite sample has 8.53 per cent porosity. The porosity increases with the increase in HA weight percentage. Table II also presents the percentage of porosity generated in the composite structure. The relative density was measured by mass per unit volume and obtained in the range of 87-97 per cent. The density decreases with the increase in HA weight percentage.

Figure 5 shows the XRD pattern of the sintered composites. It can be clearly seen that Mg-3Si-HA composites have same pattern, although their relative intensity of HA changes with HA content in the composite. Mg-3Si-HA shows the formation of MgCaO, CaMgSi and Mg<sub>2</sub>Si phases, whereas Mg-3Si composite shows the formation of Mg<sub>2</sub>Si phases. Mg<sub>2</sub>Si phases are expected to enhance corrosion resistance, whereas CaMgSi and MgCaO are beneficial for the apatite growth and improve the bioactivity.

### 3.2 Mechanical properties

Figure 6 shows the distinctive loading/unloading plot and indent image for the all sintered compacts. As depicted from the plots, the slope of the unloading curves of Mg-3Si composite sample is less than the Mg-3Si-5HA and Mg-3Si-10HA composite samples. This means that Mg-3Si composite samples have less penetration among all three samples, which indicates that samples have high hardness. Correspondingly, the Mg-3Si composite sample has high elastic modulus. This is because the reinforcement of Si element and Si element has high

| Samples     | Theoretical density (gm/cm <sup>3</sup> ) | Measured density (gm/cm <sup>3</sup> ) | Relative density (%) | Porosity (%) |
|-------------|---|--|----------------------|--------------|
| Mg-3Si      | 1.72                                      | 1.66 ± 0.05                            | 96.50                | 3.5          |
| Mg-3Si-5HA  | 1.76                                      | 1.61 ± 0.05                            | 91.47                | 8.53         |
| Mg-3Si-10HA | 1.80                                      | 1.57 ± 0.05                            | 87.20                | 12.8         |

**Table III.**  
Theoretical and measured density of all composites

hardness, which increases the brittleness of the compact. As a result, high hardness and elastic moduli were obtained. On the other hand, the slope of the unloading curves of Mg-3Si-10HA composite sample is high in compression to Mg-3Si-5HA and Mg-3Si composite samples. This revealed that the Mg-3Si-10HA composite sample has highest penetration,

**Figure 5.**  
X-ray diffraction  
patterns of sintered  
compacts

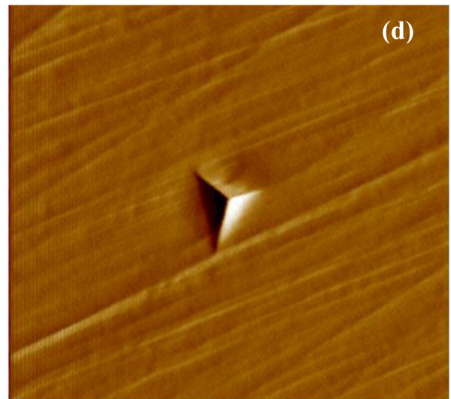
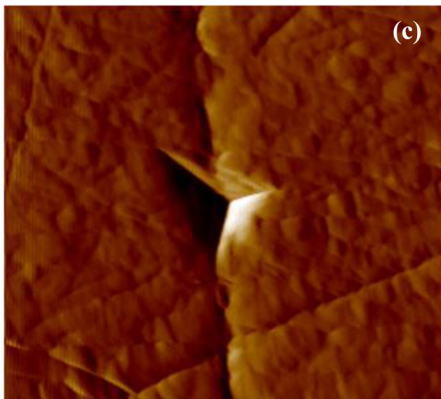
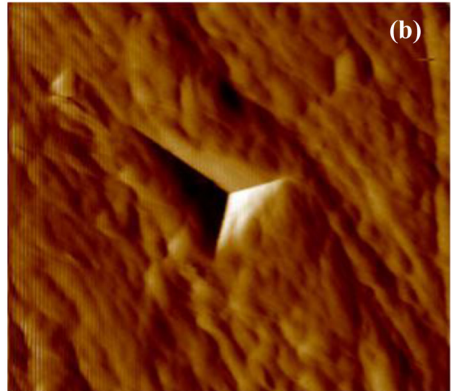
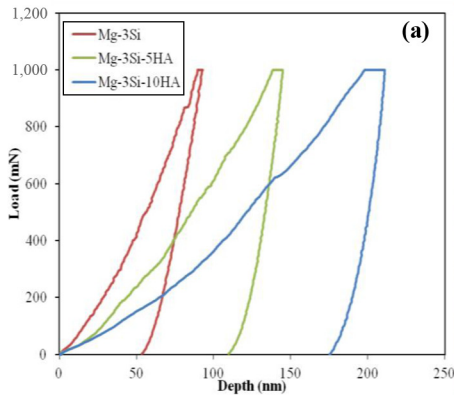
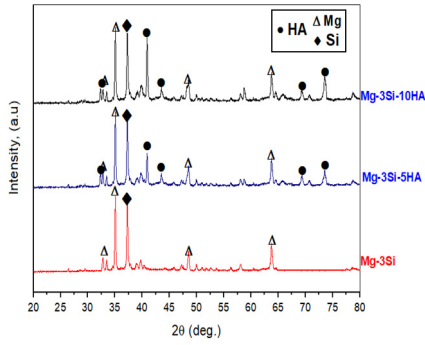


**Figure 6.**  
Loading-unloading  
depth profile and  
indentation  
impression on  
sintered composites

which indicates that the hardness of sample is less than others. This is because the reinforcement of HA element and HA element creates porosity in the structure, which further reduces the mechanical properties of compact. The Mg-3Si-10HA composite sample has low hardness and as a result of this low elastic moduli of approximately 32 GPa (near to bone) were obtained. It is evident from the indented image that the Mg-3Si-10HA composite sample has a low hardness, as the size of the indent is small as compared to the indent size of the Mg-3Si-5HA and Mg-3Si composite samples. Table IV presents mechanical properties of all three composite composites.

### 3.3 Electrochemical measurements

*In-vitro* corrosion evaluation of the as-fabricated composites was conducted via potentiodynamic polarization in Ringer's solution (SBF). Figure 7 shows the Tafel polarization graph of three composite samples fabricated at sintering pressure of 40 MPa and temperature of 400 K. Table V outlined the corrosion parameters – potential ( $E_{corr}$ ), corrosion current density ( $I_{corr}$ ), polarization resistance ( $R_p$ ) and corrosion rate ( $C_R$ ). The results showed the  $E_{corr}$  in the case of Mg-3Si composite was about  $-1.27$  mV and relative  $I_{corr}$  was  $125 \mu\text{A}/\text{cm}^{-2}$ , caused active degradation of the substrate. The corrosion rate for Mg-3Si was measured to be about 2.05 mm/year. The developed passive layer was less defensive and precarious and thus the composite degraded rapidly. Comparatively, it has been found that the corrosion potential of the Mg-3Si-5HA and Mg-3Si-10HA composite specimens is  $-1.21$  and  $-1.25$ , respectively. Furthermore, the hyperbolic curve for the as-fabricated Mg-3Si-5HA and Mg-3Si-10HA composite specimens was shifted toward a lower

| Mg-alloys   | Elastic modulus, E (GPa) | Mechanical properties |                  |
|-------------|--------------------------|-----------------------|------------------|
|             |                          | Hardness, H (GPa)     | Hardness, H (HV) |
| Mg-3Si      | 45                       | 1.97                  | 200              |
| Mg-3Si-5HA  | 39                       | 1.18                  | 120              |
| Mg-3Si-10HA | 32                       | 0.54                  | 55               |

**Table IV.**  
Elastic modulus and  
hardness of the  
sintered  
biocomposite

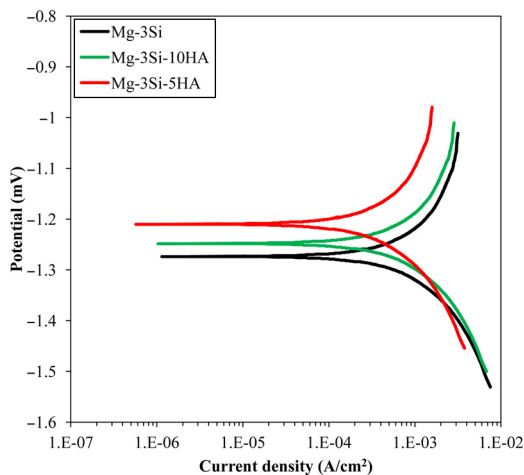


**Figure 7.**  
Potentiodynamic  
polarization curves of  
Mg-3Si, Mg-3Si-5HA  
and Mg-3Si-10HA  
composites in SBF  
(Ringer's Solution) at  
( $37 \pm 1$ )°C

current density side and corresponding current density was measured approximately 75 and 98  $\mu A/cm^{-2}$ . In Mg-3Si composites, Si reinforcement particles helped in the formation of  $MgSi_2$ , a corrosion resistive phase, as reported elsewhere []. In Mg-3Si-HA, the alloying of HA and Si has resulted into formation of corrosion barriers phases ( $CaMg$ ,  $MgSi_2$  and  $CaMgSi$ ). In the case of as-sintered Mg-3Si-HA composite, the corrosion resistance was found to be highest as the dual alloying of HA and Si produced desirable. With the alloying of HA in Mg-3Si composite, the degradation rate of was reduced by 41.95 per cent times from 2.05 mm/year to 1.19 mm/year.

3.4 Degradation analysis

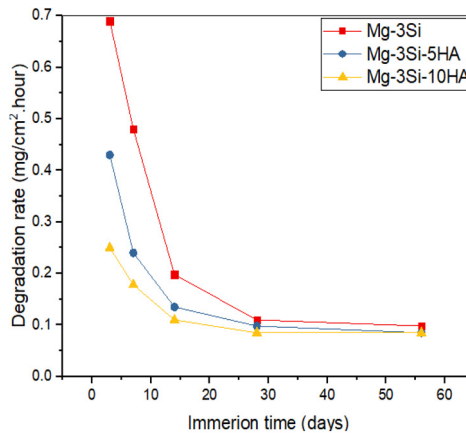
Figure 8 presents the degradation rate of as-fabricated Mg-composites in SBF solution for 3, 7, 14, 28 and 56 days. Initially, the degradation rate of Mg-3Si composite is high as compared to Mg-3Si-HA composites samples, but after 28 days of immersion, it becomes approximately contact till 56 days. The Mg-3Si-5HA composite samples have less degradation rate and high apatite growth level as compared to the Mg-3Si composite samples. The high apatite growth level reduced the degradation rate of the Mg-3Si-5HA composite samples. The weight percentage of HA and density of as-fabricated composite greatly affect the growth of apatite layer formation. When 10 per cent HA was used as reinforcement, the rate of mass deposition of apatite layer was high with high apatite growth level as compared to the Mg-3Si-5HA composite samples. But the apatite layer was shredded because of being highly porous in nature and degradation took place in the form of pulverized fine particles. Figure 9 presents the degraded surface morphology of the as-fabricated composites after immersed in SBF solution for 28 days. The Mg-3Si composite

Table V.

Corrosion parameters determined by Tafel extrapolation method

| Parameters                  | Mg alloys |            |             |
|-----------------------------|-----------|------------|-------------|
|                             | Mg-3Si    | Mg-3Si-5HA | Mg-3Si-10HA |
| $I_{corr}$ ( $\mu A/cm^2$ ) | 125       | 75         | 98          |
| $E_{corr}$ (mV)             | -1.27     | -1.25      | -1.21       |
| $C_R$ (mm/year)             | 2.05      | 1.19       | 1.62        |

Figure 8. Degradation rate of compositions as a function of time in SBF immersion



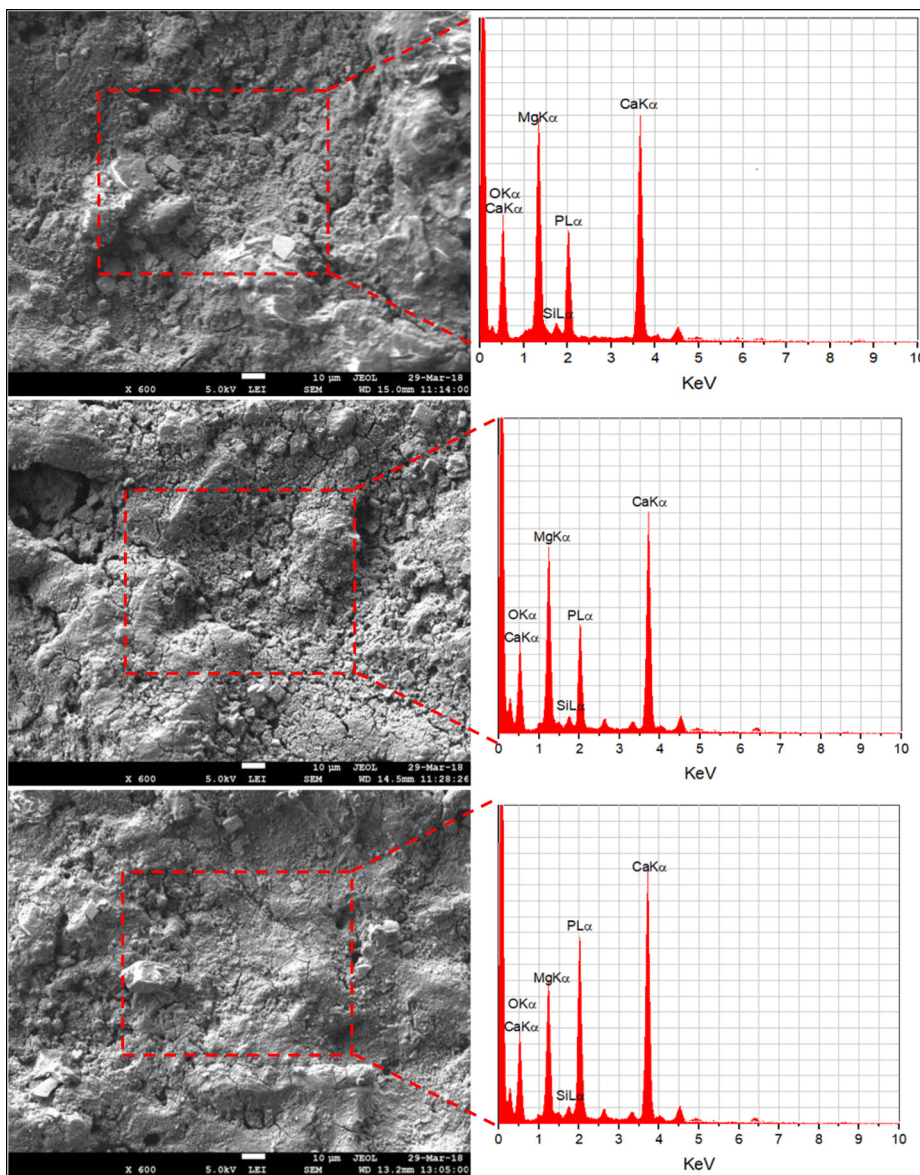


**Figure 9.**  
SEM micrograph  
shows the degraded  
morphology of  
composite structures  
for 28 days in SBF  
immersion

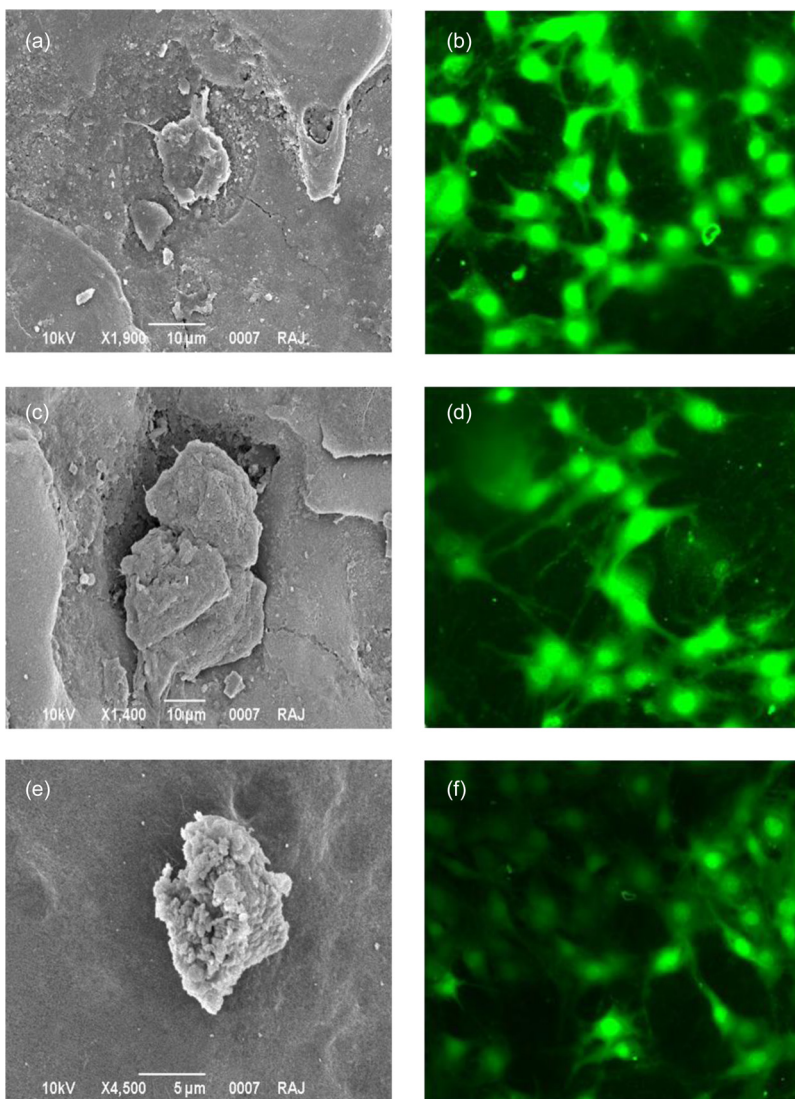
surface was highly corroded. The shredding of apatite can be clearly seen in the form of hole and crack. The traces of pulverized fine particles apatite layer in the form of Ca and P were observed, as can be seen in the EDS spectrum. The associated EDS spectrum confirmed the presence of Ca, P, O and Mg on the degradation surface, which revealed the formation of apatite growth on the composite samples. On the other hand, Mg-3Si-HA composite specimen surface has less corroded as compared with Mg-3Si composite, this is because HA

helps to form a thick layer of apatite on the composite, which further prevents the surface from degradation/corrosion. The apatite layer formation on the Mg-3Si-5HA composite was higher than on Mg-3Si-10HA. The associated EDS spectrum confirmed the presence of Ca, P, O and Mg on the degradation surface, which revealed the formation of apatite growth on the composite samples. The peak intensity of Ca and P is higher than the Mg, which further revealed the formation of apatite layer on the surface. The apatite layer formed on Mg-3Si-10HA was high porous and detached in the form of pulverized particles, which degraded the corrosion resistance and degraded the composite. Very big open holes due to release of  $H_2$  gas and  $Mg^{2+}$  ions can be clearly seen on the surface.

### 3.5 *In-vitro* biocompatibility assessments

Figure 10(a), (c) and (e) shows the SEM micrograph of the attached cells. It has been clearly seen that the cells have polygonal shape and start to proliferate after 24 h. Biological activities like cytoplasmic extensions, the accusation of filopodia and retraction of ECM activity indicating the cell spreading on all specimens' surfaces were clearly observed. Figure 10(b), (d) and (f) shows the fluorescent images of the live cells of MG-63 on the specimen surfaces. In all cases, the surfaces exhibited a significant amount of MG-63 live cells (green), and it can be said that the composites are suitable for the growth of osteoblast-like cells. It was observed that Mg-3Si-5HA surface exhibits higher density of live cells as compared to Mg-3Si and Mg-3Si-10HA. It appears that the polygonal morphology with filopodias of the attached cells established sound mechanical anchorage with the composite surface. The formation of these biological activities on the composite surface revealed that the adhesion and proliferation of Mg-63 cells are supportive and active. Hence, the as-sintered composites are favorable for the growth, proliferation, metabolic activities and differentiation of osteoblastic cells. Figure 11 shows the cell viability assessed by various assays: cell counting, MTT assay and DNA content evaluation. Figure 11(a) shows the number of cells on the as-sintered composites specimens. The as-sintered Mg-3Si-5HA composite specimens showed higher number of cells in comparison to Mg-3Si and Mg-3Si-10HA composite specimens. Evidentially, it was seen that the density of cell increased by increasing the incubation time for all types of specimens, which further enhanced the degree of cell attachment on the surface. Figure 11(b) illustrates the observations of cell proliferation of MG-63 osteoblast-like cells on Mg-3Si, Mg-3Si-10HA and Mg-3Si-5HA specimen according to the MTT assay.

The Mg-3Si-5HA composite specimens have better cell proliferation rate. This is ascribed because of the presence of Si and HA element along with high-degree of porosity in structure. It was reported that Si and HA enhanced the bone formation process. Moreover, the structural porosities created super-hydrophobic surface, which enhanced the surface energy and bioactivity of the composite. This leads to stimulate protein absorption resulting in enhancement of cell attachment and proliferation. Figure 11(c) shows the DNA content by MG-63 cells grown on all composite specimens. The results revealed that the DNA content was proportional to cell proliferation on all types of specimen's surfaces. Higher degrees of cell attachment and proliferation led to a higher DNA content. The Mg-3Si-5HA composite has high content of DNA. The differentiation of Mg-63 cells was evaluated using ALP activity at one day, three days and seven days on all types of specimen, as shown in Figure 11(d). It can be clearly observed that the ALP activity increased significantly as the culture time period increased. A significantly higher level of ALP activity by MG-63 cells was observed on Mg-3Si-5HA composite specimens as compared to Mg-3Si and Mg-3Si-10HA specimen after seven days of growth.



**Notes:** (a and b) Mg-3Si; (c and d) Mg-3Si-5HA; (e and f) Mg-3Si-10HA composite surface

**Figure 10.**  
Adhesion  
characteristics of  
MG-63 cell after 24 h  
in culture

#### 4. Conclusions

Potential application of MA-SPS technique was considered for the design and development of new low elastic porous Mg-3Si-HA composites with improved mechanical integrity, corrosion resistance properties and biocompatibility. The following conclusions were drawn from the present study:

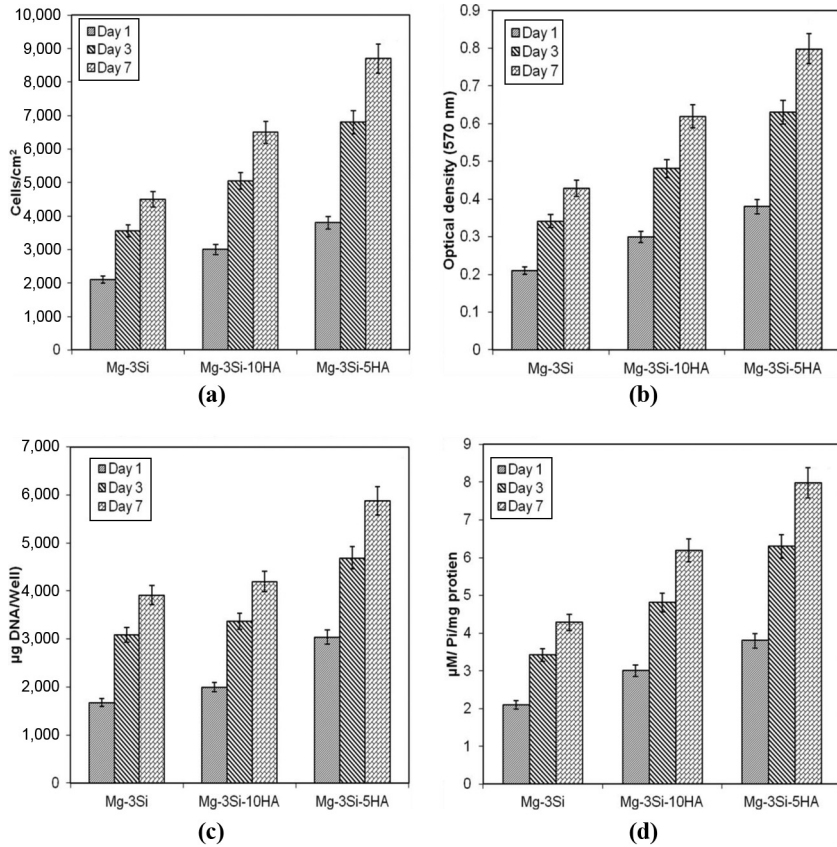


**Figure 11.**  
Cell proliferation and differentiation results

**Notes:** (a) Number of cell; (b) MTT assay; (c) DNA content; (d) ALP activity of MG-63 cells determined on Days 1, 3 and 7 after seeding on Mg-3Si, Mg-3Si-5HA and Mg-3Si-10HA composites

- The reinforcement of HA primarily leads to the formation of biomimetic porous structure in the compact and biocompatible phases such as CaMg, MgSi<sub>2</sub> and CaMgSi in the porous layers, which enhanced the corrosion resistance and bioactivity of the as-sintered composites.
- HA and Si powders when combined enhanced the mechanical properties of Mg composite. Furthermore, the developed composites structures attained reasonable hardness ranging from 86 to 200 HV and Young's moduli ranging from 29 to 45 GPa. The Mg-3Si-5HA composite exhibited lowest Young's moduli of approximately 32 GPa close to nature bone (30 GPa).
- Adequate amount of HA reinforcement (5 per cent) reduced the degradation rate of Mg-3Si composite and improved the corrosion properties. The degradation rate of Mg-3Si composite was reduced by 41.95 per cent times from 2.05 mm/year to 1.19 mm/year.

- The *in-vitro* bioactivity results indicated that the Mg-3Si-5HA composite had excellent biocompatibility and promotes cell adhesion, growth, proliferation and differentiation.

Moreover, the combination of low elastic modulus, high corrosion resistance and enhanced bioactivity might make porous Mg-3Si-HA composites prepared by MA-SPS a promising candidate for orthopedic applications as screw, plates and bio-inserts. The future work may focus on the control of the pore size, consistency and development of customized architectures to fulfill a wide range of applications. Along with this, clinical trials are also necessary for statistical analysis of *in-vivo* results to meet up all the claims.

Future directions of the present research will deal with studies on the mechanical modeling and the employment of biodegradable Mg-3Si-5HA composites for the manufacturing of a wide range of multiscale composite materials and structures with arbitrary geometry at different scales (Feo *et al.*, 2017; Mosallam and Nasr, 2017).

## References

- Ben-Hamu, G., Eliezer, D. and Shin, K.S. (2007), "The role of Si and Ca on new wrought Mg-Zn-Mn based alloy", *Materials Science and Engineering: A*, Vol. 447 Nos 1/2, pp. 35-43.
- Cao, N.Q., Pham, D.N., Kai, N., Dinh, H.V., Hiromoto, S. and Kobayashi, E. (2017), "In vitro corrosion properties of Mg matrix in situ composites fabricated by spark plasma sintering", *Metals*, Vol. 7 No. 9, p. 358.
- Carni, D.L., Scuro, C., Lamonaca, F., Olivito, R.S. and Grimaldi, D. (2017), "Damage analysis of concrete structures by means of acoustic emissions technique", *Composites Part B: Engineering*, Vol. 115, pp. 79-86.
- Chen, H.B., Kai, T., Bin, Y. and Zhang, J.S. (2009), "Nanostructured Al-Zn-Mg-Cu alloy synthesized by cryomilling and spark plasma sintering", *Transactions of Nonferrous Metals Society of China*, Vol. 19 No. 5, pp. 1110-1115.
- Cheng, Y., Cui, Z., Cheng, L., Gong, D. and Wang, W. (2017), "Effect of particle size on densification of pure magnesium during spark plasma sintering", *Advanced Powder Technology*, Vol. 28 No. 4, pp. 1129-1135.
- Ermakova, A. and Dayyani, I. (2017), "Shape optimisation of composite corrugated morphing skins", *Composites Part B: Engineering*, Vol. 115, pp. 87-101.
- Feo, L., Fraternali, F. and Skelton, R.E. (2017), "Special issue on composite lattices and multiscale innovative materials and structures", *Composites Part B: Engineering*, Vol. 115, pp. 1-2.
- Feo, L., Latour, M., Penna, R. and Rizzano, G. (2017), "Pilot study on the experimental behavior of GFRP-steel slip-critical connections", *Composites Part B: Engineering*, Vol. 115, pp. 209-222.
- Fraddosio, A., Marzano, S., Pavone, G. and Piccioni, M.D. (2017), "Morphology and self-stress design of V-Expander tensegrity cells", *Composites Part B: Engineering*, Vol. 115, pp. 102-116.
- Fu, Y., Fang, H. and Dai, F. (2017), "Study on the properties of the recombinant bamboo by finite element method", *Composites Part B: Engineering*, Vol. 115, pp. 151-159.
- Fu, J., Liu, K., Du, W., Wang, Z., Li, S. and Du, X. (2017), March. "Microstructure and mechanical properties of the as-cast Mg-Zn-Mn-Ca alloys", in IOP Conference Series: Materials Science and Engineering, *IOP Publishing*, Vol. 182, No. 1, p. 012053.
- Geetha, M., Singh, A.K., Asokamani, R. and Gogia, A.K. (2009), "Ti based biomaterials, the ultimate choice for orthopaedic implants—a review", *Progress in Materials Science*, Vol. 54 No. 3, pp. 397-425.
- Ghasali, E., Alizadeh, M., Niazmand, M. and Ebadzadeh, T. (2017), "Fabrication of magnesium-boron carbide metal matrix composite by powder metallurgy route: comparison between microwave and spark plasma sintering", *Journal of Alloys and Compounds*, Vol. 697, pp. 200-207.

- Gu, X.N., Li, N., Zheng, Y.F. and Ruan, L. (2011), "In vitro degradation performance and biological response of a Mg–Zn–Zr alloy", *Materials Science and Engineering: B*, Vol. 176 No. 20, pp. 1778-1784.
- Gu, X., Zhou, W., Zheng, Y., Dong, L., Xi, Y. and Chai, D. (2010), "Microstructure, mechanical property, bio-corrosion and cytotoxicity evaluations of Mg/HA composites", *Materials Science and Engineering: C*, Vol. 30 No. 6, pp. 827-832.
- Khanra, A.K., Jung, H.C., Yu, S.H., Hong, K.S. and Shin, K.S. (2010), "Microstructure and mechanical properties of Mg-HAP composites", *Bulletin of Materials Science*, Vol. 33 No. 1, pp. 43-47.
- Knotek, V., Ekrt, O., Michalcová, A. and Vojtěch, D. (2017), "Electrochemical hydriding of nanocrystalline Mg-Ni-X (X= Co, Mn, Nd) alloys prepared by mechanical alloying and spark plasma sintering", *Journal of Alloys and Compounds*, Vol. 726, pp. 787-795.
- Knotek, V., Ekrt, O. and Vojtěch, D. (2017), "Electrochemical hydriding of Mg–Ni alloys compacted by spark plasma sintering", *International Journal of Hydrogen Energy*, Vol. 42 No. 37, pp. 23908-23914.
- Lala, S., Maity, T.N., Singha, M., Biswas, K. and Pradhan, S.K. (2017), "Effect of doping (Mg, Mn, Zn) on the microstructure and mechanical properties of spark plasma sintered hydroxyapatites synthesized by mechanical alloying", *Ceramics International*, Vol. 43 No. 2, pp. 2389-2397.
- Li, Z., Gu, X., Lou, S. and Zheng, Y. (2008), "The development of binary Mg–Ca alloys for use as biodegradable materials within bone", *Biomaterials*, Vol. 29 No. 10, pp. 1329-1344.
- Liu, X., Sun, J., Zhou, F., Yang, Y., Chang, R., Qiu, K., Pu, Z., Li, L. and Zheng, Y. (2016), "Micro-alloying with Mn in Zn–Mg alloy for future biodegradable metals application", *Materials and Design*, Vol. 94, pp. 95-104.
- Mosallam, A.S. and Nasr, A. (2017), "Structural performance of RC shear walls with post-construction openings strengthened with FRP composite laminates", *Composites Part B: Engineering*, Vol. 115, pp. 488-504.
- Narita, K., Kobayashi, E. and Sato, T. (2016), "Sintering behavior and mechanical properties of magnesium/ $\beta$ -Tricalcium Phosphate composites sintered by spark plasma sintering", *Materials Transactions*, Vol. 57 No. 9, pp. 1620-1627.
- Oliver, W.C. and Pharr, G.M. (1992), "An improved technique for determining hardness and elastic modulus using load and displacement sensing indentation experiments", *Journal of Materials Research*, Vol. 7 No. 6, pp. 1564-1583.
- Prakash, C., Kansal, H.K., Pabla, B.S., Puri, S. and Aggarwal, A. (2016), "Electric discharge machining—a potential choice for surface modification of metallic implants for orthopedic applications: a review", *Proceedings of the Institution of Mechanical Engineers, Part B: Journal of Engineering Manufacture*, Vol. 230 No. 2, pp. 331-353.
- Prakash, C. and Uddin, M.S. (2017), "Surface modification of  $\beta$ -phase Ti implant by hydroxyapatite mixed electric discharge machining to enhance the corrosion resistance and in-vitro bioactivity", *Surface and Coatings Technology*, Vol. 326, pp. 134-145.
- Queudet, H., Lemonnier, S., Barraud, E., Guyon, J., Ghanbaja, J., Allain, N. and Gaffet, E. (2017), "One-step consolidation and precipitation hardening of an ultrafine-grained Al–Zn–Mg alloy powder by spark plasma sintering", *Materials Science and Engineering: A*, Vol. 685, pp. 227-234.
- Radha, R. and Sreekanth, D. (2017), "Insight of magnesium alloys and composites for orthopedic implant applications – a review", *Journal of Magnesium and Alloys 5*, Vol. 5 No. 3, pp. 286-312.
- Rudinsky, S., Hendrickx, P., Bishop, D.P. and Brochu, M. (2016), "Spark plasma sintering and age hardening of an Al–Zn–Mg alloy powder blend", *Materials Science and Engineering: A*, Vol. 650, pp. 129-138.
- Singh, N., Hui, D., Singh, R., Ahuja, I.P.S., Feo, L. and Fraternali, F. (2017), "Recycling of plastic solid waste: a state of art review and future applications", *Composites Part B: Engineering*, Vol. 115, pp. 409-422.

- Singh, R., Singh, R., Dureja, J.S., Farina, I. and Fabbrocino, F. (2017), "Investigations for dimensional accuracy of Al alloy/Al-MMC developed by combining stir casting and ABS replica based investment casting", *Composites Part B: Engineering*, Vol. 115, pp. 203-208.
- Singh, B.P., Singh, R., Mehta, J.S. and Prakash, C. (2017), August. "Fabrication of biodegradable low elastic porous Mg-Zn-Mn-HA alloy by spark plasma sintering for orthopaedic applications", in IOP Conference Series: Materials Science and Engineering, *IOP Publishing*, Vol. 225, No. 1, p. 012050.
- Song, G. (2007), "Control of biodegradation of biocompatible magnesium alloys", *Corrosion Science*, Vol. 49 No. 4, pp. 1696-1701.
- Spoerke, E.D., Murray, N.G., Li, H., Brinson, L.C., Dunand, D.C. and Stupp, S.I. (2005), "A bioactive titanium foam scaffold for bone repair", *Acta Biomaterialia*, Vol. 1 No. 5, pp. 523-533.
- Staiger, M.P., Pietak, A.M., Huadmai, J. and Dias, G. (2006), "Magnesium and its alloys as orthopedic biomaterials: a review", *Biomaterials*, Vol. 27 No. 9, pp. 1728-1734.
- Sunil, B.R., Ganapathy, C., Kumar, T.S. and Chakkingal, U. (2014), "Processing and mechanical behavior of lamellar structured degradable magnesium-hydroxyapatite implants", *Journal of the Mechanical Behavior of Biomedical Materials*, Vol. 40, pp. 178-189.
- Talò, M., Krause, B., Pionteck, J., Lanzara, G. and Lacarbonara, W. (2017), "An updated micromechanical model based on morphological characterization of carbon nanotube nanocomposites", *Composites Part B: Engineering*, Vol. 115, pp. 70-78.
- Tünçay, M.M., Muñiz-Lerma, J.A., Bishop, D.P. and Brochu, M. (2017), "Spark plasma sintering and spark plasma upsetting of an Al-Zn-Mg-Cu alloy", *Materials Science and Engineering: A*, Vol. 704, pp. 154-163.
- Uddin, M.S., Hall, C. and Murphy, P. (2015), "Surface treatments for controlling corrosion rate of biodegradable Mg and Mg-based alloy implants", *Science and Technology of Advanced Materials*, Vol. 16 No. 5, p. 053501.
- Uddin, M.S., Rosman, H., Hall, C. and Murphy, P. (2017), "Enhancing the corrosion resistance of biodegradable Mg-based alloy by machining-induced surface integrity: influence of machining parameters on surface roughness and hardness", *The International Journal of Advanced Manufacturing Technology*, Vol. 90 Nos 5/8, pp. 2095-2108.
- Vahidgolpayegani, A., Wen, C., Hodgson, P. and Li, Y. (2017), "Production methods and characterization of porous Mg and Mg alloys for biomedical applications", in *Metallic Foam Bone*, Woodhead Publishing, Duxford, pp. 25-82.
- Zhang, W., Li, M., Chen, Q., Hu, W., Zhang, W. and Xin, W. (2012), "Effects of Sr and Sn on microstructure and corrosion resistance of Mg-Zr-Ca magnesium alloy for biomedical applications", *Materials and Design*, Vol. 39, pp. 379-383.
- Zhang, S., Li, J., Song, Y., Zhao, C., Zhang, X., Xie, C., Zhang, Y., Tao, H., He, Y., Jiang, Y. and Bian, Y. (2009), "In vitro degradation, hemolysis and MC3T3-E1 cell adhesion of biodegradable Mg-Zn alloy", *Materials Science and Engineering: C*, Vol. 29 No. 6, pp. 1907-1912.
- Zhang, X., Wang, Z., Yuan, G. and Xue, Y. (2012), "Improvement of mechanical properties and corrosion resistance of biodegradable Mg-Nd-Zn-Zr alloys by double extrusion", *Materials Science and Engineering: B*, Vol. 177 No. 13, pp. 1113-1119.
- Zhang, E., Yang, L., Xu, J. and Chen, H. (2010), "Microstructure, mechanical properties and bio-corrosion properties of Mg-Si (-Ca, Zn) alloy for biomedical application", *Acta Biomaterialia*, Vol. 6 No. 5, pp. 1756-1762.
- Zhang, E., Yin, D., Xu, L., Yang, L. and Yang, K. (2009), "Microstructure, mechanical and corrosion properties and biocompatibility of Mg-Zn-Mn alloys for biomedical application", *Materials Science and Engineering: C*, Vol. 29 No. 3, pp. 987-993.
- Zhang, H., Zhao, Y., Yan, Y., Fan, J., Wang, L., Dong, H. and Xu, B. (2017), "Microstructure evolution and mechanical properties of Mg matrix composites reinforced with Al and nano SiC particles

using spark plasma sintering followed by hot extrusion”, *Journal of Alloys and Compounds*, Vol. 725, pp. 652-664.

Zheng, B., Ertorer, O., Li, Y., Zhou, Y., Mathaudhu, S.N., Tsao, C.Y. and Lavernia, E.J. (2011), “High strength, nano-structured Mg–Al–Zn alloy”, *Materials Science and Engineering: A*, Vol. 528 Nos 4/5, pp. 2180-2191.

### Further reading

Alessi, R., Favata, A. and Micheletti, A. (2017), “Pressurized CNTs under tension: a finite-deformation lattice model”, *Composites Part B: Engineering*, Vol. 115, pp. 223-235.

Amendola, A., Benzoni, G. and Fraternali, F. (2017), “Non-linear elastic response of layered structures, alternating pentamode lattices and confinement plates”, *Composites Part B: Engineering*, Vol. 115, pp. 117-123.

American Society for Testing and Materials (1999), Annual Book of ASTM Standards, ASTM, Designation: G102-89.

Bacigalupo, A., Gnecco, G., Lepidi, M. and Gambarotta, L. (2017), “Optimal design of low-frequency band gaps in anti-tetrachiral lattice Meta-materials”, *Composites Part B: Engineering*, Vol. 115, pp. 341-359.

Bieniek, Z. (2017), “The self-equilibrium problem of the Class-Theta tetrahedral tensegrity module”, *Composites Part B: Engineering*, Vol. 115, pp. 21-29.

Blesgen, T. (2017), “A variational model for dynamic recrystallization based on cosserat plasticity”, *Composites Part B: Engineering*, Vol. 115, pp. 236-243.

Brighenti, R. and Vernerey, F.J. (2017), “A simple statistical approach to model the time-dependent response of polymers with reversible cross-links”, *Composites Part B: Engineering*, Vol. 115, pp. 257-265.

Cao, N.Q., Narita, K., Kobayashi, E. and Sato, T. (2016), “Evolution of the microstructure and mechanical properties of Mg-matrix in situ composites during spark plasma sintering”, *Powder Metallurgy*, Vol. 59 No. 5, pp. 302-307.

Carpentieri, G. and Skelton, R.E. (2017), “On the minimal mass design of composite membranes”, *Composites Part B: Engineering*, Vol. 115, pp. 244-256.

Castaldo, P., Natri, E. and Piluso, V. (2017), “FEM simulations and rotation capacity evaluation for RHS temper T4 aluminium alloy beams”, *Composites Part B: Engineering*, Vol. 115, pp. 124-137.

Castaldo, P., Palazzo, B., Ferrentino, T. and Petrone, G. (2017), “Influence of the strength reduction factor on the seismic reliability of structures with FPS considering intermediate PGA/PGV ratios”, *Composites Part B: Engineering*, Vol. 115, pp. 308-315.

Cimmino, M.C., Miranda, R., Sicignano, E., Ferreira, A.J.M., Skelton, R.E. and Fraternali, F. (2017), “Composite solar façades and wind generators with tensegrity architecture”, *Composites Part B: Engineering*, Vol. 115, pp. 275-281.

Colangelo, F. and Cioffi, R. (2017), “Mechanical properties and durability of mortar containing fine fraction of demolition wastes produced by selective demolition in South Italy”, *Composites Part B: Engineering*, Vol. 115, pp. 43-50.

Cullity, B.D. (1957), “Elements of X-Ray Diffraction”, *American Journal of Physics*, Vol. 25 No. 6, p. 394.

Cuomo, M., Dell’Isola, F., Greco, L. and Rizzi, N.L. (2017), “First versus second gradient energies for planar sheets with two families of inextensible fibres: Investigation on deformation boundary”, *Composites Part B: Engineering*, Vol. 115, pp. 423-448.

De Tommasi, D., Marano, G.C., Puglisi, G. and Trentadue, F. (2017), “Morphological optimization of tensegrity-type metamaterials”, *Composites Part B: Engineering*, Vol. 115, pp. 182-187.

Fabbrocino, F., Farina, I. and Modano, M. (2017), “Loading noise effects on the system identification of composite structures by dynamic tests with vibrodyne”, *Composites Part B: Engineering*, Vol. 115, pp. 376-383.

- 
- Fantilli, A.P., Frigo, B. and Chiaia, B. (2017), "Comparing multi-scale cracking mechanisms in man-made composites and natural materials", *Composites Part B: Engineering*, Vol. 115, pp. 369-375.
- Fantuzzi, N., Tornabene, F., Baccocchi, M. and Dimitri, R. (2017), "Free vibration analysis of arbitrarily shaped functionally graded carbon nanotube-reinforced plates", *Composites Part B: Engineering*, Vol. 115, pp. 384-408.
- Ferrante Cavallaro, G., Francavilla, A., Latour, M., Piluso, V. and Rizzano, G. (2017), "Experimental behaviour of innovative thermal spray coating materials for FREEDAM joints", *Composites Part B: Engineering*, Vol. 115, pp. 289-299.
- Genoese, A., Genoese, A., Rizzi, N.L. and Salerno, G. (2017), "On the derivation of the elastic properties of lattice nanostructures: the case of graphene sheets", *Composites Part B: Engineering*, Vol. 115, pp. 316-329.
- Jamesh, M., Kumar, S. and Narayanan, T.S. (2012), "Electrodeposition of hydroxyapatite coating on magnesium for biomedical applications", *Journal of Coatings Technology and Research*, Vol. 9 No. 4, pp. 495-502.
- Khezzzadeh, H. (2017), "A statistical micromechanical multiscale method for determination of the mechanical properties of composites with periodic microstructure", *Composites Part B: Engineering*, Vol. 115, pp. 138-143.
- Lucantonio, A., Tomassetti, G. and De Simone, A. (2017), "Large-strain poroelastic plate theory for polymer gels with application to swelling-induced morphing of composite plates", *Composites Part B: Engineering*, Vol. 115, pp. 330-340.
- Magliozzi, L., Micheletti, A., Pizzigoni, A. and Ruscica, G. (2017), "On the design of origami structures with a continuum of equilibrium shapes", *Composites Part B: Engineering*, Vol. 115, pp. 144-150.
- Minafò, G., D'Anna, J., Cucchiara, C., Monaco, A. and La Mendola, L. (2017), "Analytical stress-strain law of FRP confined masonry in compression: Literature review and design provisions", *Composites Part B: Engineering*, Vol. 115, pp. 160-169.
- Monaco, A., Minafò, G., Cucchiara, C., D'Anna, J. and La Mendola, L. (2017), "Finite element analysis of the out-of-plane behavior of FRP strengthened masonry panels", *Composites Part B: Engineering*, Vol. 115, pp. 188-202.
- Montuori, R. and Muscati, R. (2017), "Smart and simple design of seismic resistant reinforced concrete frame", *Composites Part B: Engineering*, Vol. 115, pp. 360-368.
- Naddeo, F., Naddeo, A. and Cappetti, N. (2017), "Novel 'load adaptive algorithm based' procedure for 3D printing of cancellous bone-inspired structures", *Composites Part B: Engineering*, Vol. 115, pp. 60-69.
- Naddeo, F., Naddeo, A. and Cappetti, N. (2017), "Novel 'load adaptive algorithm based' procedure for 3D printing of lattice-based components showing parametric curved micro-beams", *Composites Part B: Engineering*, Vol. 115, pp. 51-59.
- Papa, I., Lopresto, V., Simeoli, G., Langella, A. and Russo, P. (2017), "Ultrasonic damage investigation on woven jute/poly (lactic acid) composites subjected to low velocity impact", *Composites Part B: Engineering*, Vol. 115, pp. 282-288.
- Rimoli, J.J. and Pal, R.K. (2017), "Mechanical response of 3-dimensional tensegrity lattices", *Composites Part B: Engineering*, Vol. 115, pp. 30-42.
- Sheikholeslami, S.A., Aghdam, M.M., Zappino, E. and Carrera, E. (2017), "Application of refined beam elements to the coupled-field analysis of magnetostrictive microbeams", *Composites Part B: Engineering*, Vol. 115, pp. 14-20.
- Shen, Y., Huang, D., Zhou, A. and Hui, D. (2017), "An inelastic model for ultimate state analysis of CFRP reinforced PSB beams", *Composites Part B: Engineering*, Vol. 115, pp. 266-274.
- Shirinbayan, M., Fitoussi, J., Bocquet, M., Meraghni, F., Surowiec, B. and Tcharkhtchi, A. (2017), "Multi-scale experimental investigation of the viscous nature of damage in advanced sheet molding

- compound (A-SMC) submitted to high strain rates”, *Composites Part B: Engineering*, Vol. 115, pp. 3-13.
- Taddei, P., Ruggiero, A., Pavoni, E. and Affatato, S. (2017), “Transfer of metallic debris after in vitro ceramic-on-metal simulation: Wear and degradation in biolox® Delta composite femoral heads”, *Composites Part B: Engineering*, Vol. 115, pp. 477-487.
- Thorhallsson, E.R., Hinriksson, G. and Snæbjornsson, J.T. (2017), “Strength and stiffness of glulam beams reinforced with glass and basalt fibres”, *Composites Part B: Engineering*, Vol. 115, pp. 300-307.
- Tornabene, F., Fantuzzi, N. and Bacciocchi, M. (2017), “Linear static response of nanocomposite plates and shells reinforced by agglomerated carbon nanotubes”, *Composites Part B: Engineering*, Vol. 115, pp. 449-476.
- Trotta, S., Marmo, F. and Rosati, L. (2017), “Evaluation of the eshelby tensor for polygonal inclusions”, *Composites Part B: Engineering*, Vol. 115, pp. 170-181.
- Zhang, L., He, Z.Y., Zhang, Y.Q., Jiang, Y.H. and Zhou, R. (2016), “Rapidly sintering of interconnected porous Ti-HA biocomposite with high strength and enhanced bioactivity”, *Materials Science and Engineering: C*, Vol. 67, pp. 104-114.
- Zheng, R., Ma, F., Xiao, W., Ameyama, K. and Ma, C. (2017), “Achieving enhanced strength in ultrafine lamellar structured Al2024 alloy via mechanical milling and spark plasma sintering”, *Materials Science and Engineering: A*, Vol. 687, pp. 155-163.

**Corresponding author**

Ilenia Farina can be contacted at: [ilenia.farina@uniparthenope.it](mailto:ilenia.farina@uniparthenope.it)